

Multi-Scale Model of Effects of Roughness on the Cohesive Strength of Self-Assembled Monolayers

Chen Zhang

*Department of Aerospace Engineering, University of Illinois at Urbana-Champaign, IL
61801, USA*

Amnaya P. Awasthi

*Department of Mechanical and Aerospace Engineering, University of Florida at Gainesville,
FL 32611, USA*

Philippe H. Geubelle*

*Department of Aerospace Engineering, University of Illinois at Urbana-Champaign, IL
61801, USA*

Jeauk Sung

*Department of Materials Science and Engineering, University of Illinois at
Urbana-Champaign, IL 61801, USA*

Nancy R. Sottos

*Department of Materials Science and Engineering, University of Illinois at
Urbana-Champaign, IL 61801, USA*

Abstract

Self-assembled monolayers (SAMs) are aggregates of small molecular chains that form highly ordered assemblies at the nanoscale. They are excellent contenders of molecular-level tailoring of interfaces because of the wide choice of terminal groups. Molecular Dynamics (MD) simulations and experimental observations of spallation of two SAM-enhanced gold-film/fused silica-substrate interfaces have shown that the cohesive strength of SAM-enriched transfer-printed interfaces is strongly dependent on the choice of terminal groups. Though the MD results of perfectly ordered atomistic surfaces show the same qualitative trend as

*Corresponding author

Email address: geubelle@illinois.edu (Philippe H. Geubelle)

the experiments, they over-predict the interfacial cohesive strengths by a factor of about 50. Previous studies have revealed that the roughness of these interfaces may significantly impact their cohesive strength. In this manuscript, we perform a multiscale study to investigate the influence of surface roughness on cohesive strength of an interface between a Si/SAM substrate and a transfer-printed gold film. We approximate the film as a 2D deformable medium while the rough SAM-enhanced substrate is modeled using 2D harmonic functions with the cohesive interaction between the SAM and the film described by MD. Spallation is simulated on this system to evaluate the effective traction-separation response for the rough SAM-gold interface. Beyond the idealized harmonic interface, we extend our studies to real surface profiles obtained by AFM. We demonstrate how interfacial roughness can reduce the cohesive strength of the SAM-enhanced interface by more than an order of magnitude.

Keywords: Self-Assembled Monolayers, Nano-Scale Interfacial Roughness, Cohesive Model, Thin Films, Spallation, Interfacial Strength.

1. Introduction

Self assembly, a common trait of biological processes, is the spontaneous interaction and organization of subunits (e.g., molecules) into stable, well-defined structures without the involvement of covalent bonding [1]. Self-assembled monolayers (SAMs) composed of short organic chains and terminated with desired functional groups are attractive for creating surface properties with desired functionalities. A large number of attractive features can be achieved using SAMs by selectively choosing their functional groups, especially for applications pertaining to molecular ordering, growth, wetting, adhesion, lubrication and corrosion [2][3][4].

The interfacial properties of SAM-enhanced systems have stimulated extensive research in the recent past. In the case of bio-compatible interfaces [5][6], synthetic interfaces with possible extensions and spreading of biological cells in different directions based on chosen SAM functional groups were produced and

examined. Losego et al. [7] investigated the effects of chemical bonding on heat transport across SAM interfaces and found that the nature of bonding between SAMs and adjacent solid layers has a major effect on the heat conductance of the interfaces. In a later study, Tian et al. [8] examined the SAM-enhanced solid-liquid interface and showed that a stronger bonding in the SAM-system causes an improved thermal transport across the solid-liquid interface. Other studies have also shown unique interfacial electrical transport properties achieved by using SAMs with different functional groups [9][10].

The focus of this manuscript is on evaluating the mechanical properties of SAM-enhanced film/substrate interfaces, where SAMs provide an enabling platform for molecular tailoring of interfacial adhesion. The use of SAMs to alter interfacial mechanical properties has been investigated on the molecular scale using scanning force microscopy [11]. Related studies include the work of Bush et al. [12], who measured the elastic modulus, work of adhesion and interfacial shear strength of methyl-terminated alkylsilane SAMs through scanning probe normal and lateral force measurements. Kent et al. [13] varied the type and density of interfacial interactions between epoxy and silicon using mixed monolayers of weak methyl-terminated dodecyltrichlorosilane (DTS) and strong bromo-undecyltrichlorosilane (BrUTS). Zhuk et al. [14] investigated the dependence of the work of adhesion on the ratio of COOH/CH₃ functional groups at the interface between an epoxy film and a SAM modified Au/Ti/Si substrate. Owing to the small size and structured feature of SAMs, molecular dynamics (MD) simulations have also been used to study the interfacial mechanical properties of SAM-modified interfaces. Siepmann and McDonald [15] studied the mechanical relaxation of an alkanethiol SAM on gold, subjected to compression. Tupper and Brenner [16] simulated the structural transition of n-hexadecanethiol SAMs on Au during compression. Lane et al. [17] modeled the interaction between water molecules and SAMs and measured the degree of water penetration depending on different initial damage to the SAMs.

SAM-modified interfaces are not perfectly flat, and rough SAM surfaces are frequently encountered in real devices [18]. Based on the nature of the sub-

strate and the polishing techniques, SAMs may exhibit rms roughness values ranging from a few to tens of nanometers [19][20], surpassing the chain length of SAM molecules. This roughness profile can significantly affect the formation of SAMs, reduce the effective contact area of the SAM-modified interface and negatively impact their desired interfacial properties [21][22][23]. Tupper et al. [24] and Tupper and Brenner [25] used MD to investigate the effect of the substrate roughness on the compressive response of hexadecanethiol on gold and the friction between SAMs. Ulman et al. [26] used surface force apparatus (SFA) to measure the deformation and contact forces of smooth mica and SAMs absorbed to rough gold. Their study found that the pull-off force to separate the two surfaces was dependent on the interface roughness. Xu et al. [19] investigated the adhesion force of Octadecyltriethoxysilane (OTE) SAMs on surface of crystalline Si(100) and silica nano-particle films with atomic force microscopy (AFM). Their experiment indicates that adhesion measured on OTE-modified Si(100) surfaces is approximately 15 times greater than that on rougher silica particle surfaces.

This paper is motivated by the recent work of Awasthi et al. [27], where MD simulations were performed on perfectly flat interfaces consisting of a thin gold film and various functionalized SAMs. MD simulations consistently predicted interfacial strengths of Au-SAM interfaces about 50 times higher than those measured by spallation experiments [28]. When probed by atomic force microscopy (AFM), surface roughness measurements of interacting surfaces were found to be about 1 nm, the same order of magnitude as the range of atomistic interactions. Using a continuum model of the interface between a rigid film and rough SAM-enhanced substrate, it was shown that nano-scale surface roughness significantly mitigates interfacial interactions. Therefore, the influence of surface roughness must be correctly incorporated to predict nano-scale interfacial strength. A detailed analysis of separation characteristics using a 1D continuum model of deformable film can be found in a related article [29]. In the present work, we study the behavior of a thin gold film on a SAM-modified fused silica substrate using a 2D deformable continuum representation of the film. Special

treatment is given to simulating the spallation process, evaluating the energy exchange and assessing the effective cohesive characteristics of idealized and actual SAM-enhanced interfaces.

The article is organized as follows: In Section 2, we discuss the deformation of the thin film and its initial profile after it is transfer-printed onto the SAM-enhanced substrate. In Section 3, we focus on the spallation process and evaluate the effective cohesive properties of the SAM-enhanced film/substrate interface. In Section 4, the analysis is extended to real surfaces to correlate effective cohesive properties with roughness attributes.

2. Initial Profile

2.1. Formulation

The behavior of the transfer-printed thin film is modeled by a classical thin plate model as it rests over a stiffer SAM-enhanced substrate. In this system, the SAM-enhanced substrate is idealized as a non-deformable solid. In the undeformed state, the film is assumed to be flat. In this initial study, the interface roughness is idealized as a simple harmonic function (see Section 4 for the extension to real surfaces) and the initial distance $\delta_i(x)$ between a point (x_1, x_2) on the neutral plane of the film and the rough rigid substrate is given by

$$\delta_i(x_1, x_2) = A(1 - \cos \frac{2\pi x_1}{L_1} \cos \frac{2\pi x_2}{L_2}), \quad (1)$$

with A denoting the amplitude and L_1, L_2 , the wavelength of the roughness in x_1 and x_2 directions, respectively. The transfer-printed film deforms due to cohesive interactions with the substrate. Because of its bending stiffness, the film does not completely follow the shape of the underlying profile, but rather adopts an equilibrium configuration shown in Fig. 1. For the SAM-enhanced thin film systems of interest, $A \sim 1nm$ and $L_1, L_2 \sim 500nm$ [28]. Adopting the exponential cohesive model given in [30], the cohesive traction-separation

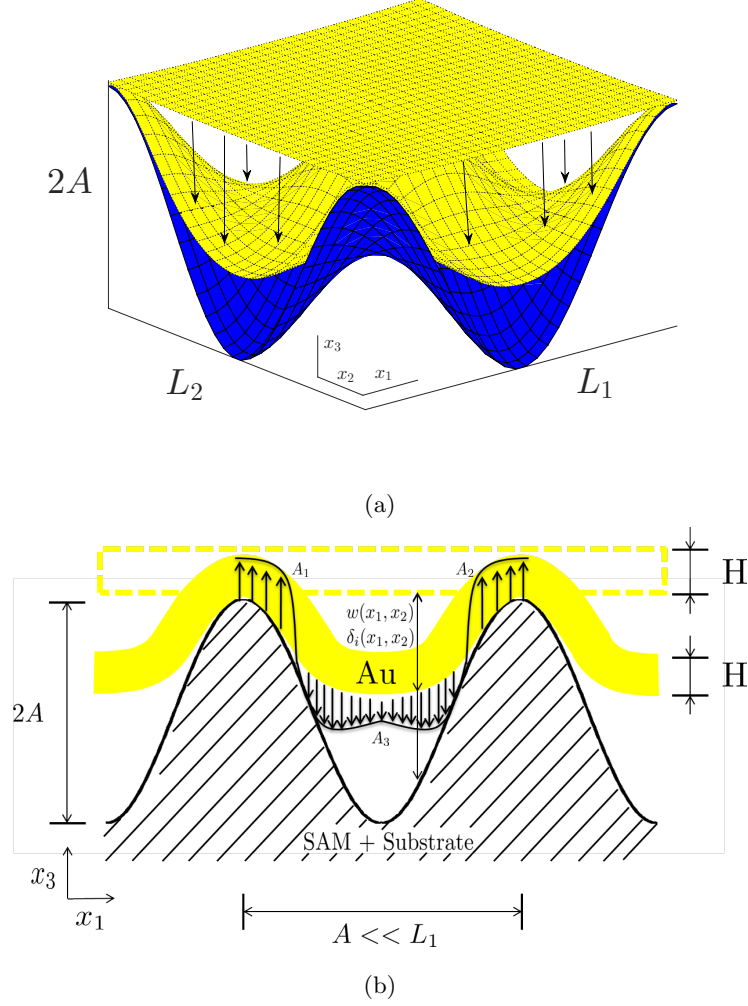


Figure 1: (a) Deformation of a deformable film (yellow) due to interaction with the SAM-enhanced substrate (blue). Note that $A \ll (L_1, L_2)$ (b) Kinematics of the film/substrate system at a planar cut, showing $\delta_i(x_1, x_2)$ and $w(x_1, x_2)$, film-substrate initial distance and film displacement at point (x_1, x_2) , respectively. $S_3(S_1$ and $S_2)$ denotes the portion of rough interface where attractive (compressive) cohesive tractions apply.

relation at the interface is expressed as

$$T_a(x_1, x_2) = \sigma_c \frac{\delta_i(x_1, x_2) + w(x_1, x_2)}{\delta_c} \exp\left[1 - \frac{\delta_i(x_1, x_2) + w(x_1, x_2)}{\delta_c}\right], \quad (2)$$

where the critical displacement jump, δ_c , and failure strength, σ_c , are obtained from molecular dynamics simulations and depend on the chemistry of interface. $\delta_i(x_1, x_2)$ is defined by (1) and $w(x_1, x_2)$ is the transverse displacement of the film, which remains to be solved. The cohesive relation in (2) is used to describe the non-contact regions where the cohesive interaction acts as an attractive force. To incorporate the compressive behavior in contact regions, a linear contact penalty under compression is adopted [31]:

$$T_c(x_1, x_2) = K_n \frac{\sigma_c}{\delta_c} (\delta_i(x_1, x_2) + w(x_1, x_2)), \quad (3)$$

where K_n is the penalty constant, chosen in this study as $K_n = 300$ to ensure convergence of the compressive force [32].

The deformation of the transfer-printed film is governed by the classical equation [33]

$$\frac{\partial^4 w(x_1, x_2)}{\partial x_1^4} + \frac{\partial^4 w(x_1, x_2)}{\partial x_2^4} + 2 \frac{\partial^4 w(x_1, x_2)}{\partial x_1^2 \partial x_2^2} = \frac{T(x_1, x_2)}{D}, \quad (4)$$

where $D = \frac{EH^3}{12(1-\nu^2)}$ with E , ν , and H denoting the Young's modulus, Poisson's ratio and thickness of the film, respectively. The cohesive traction $T(x_1, x_2)$ can be attractive or compressive and is defined by (2) and (3) in non-contact and contact regions, respectively. Let us introduce non-dimensional parameters:

$$\begin{aligned} \tilde{x}_1 &= \frac{x_1}{L_1}, \quad \tilde{x}_2 = \frac{x_2}{L_2}, \quad \eta = \frac{A}{\delta_c}, \quad \tilde{w} = \frac{w}{A}, \\ \tilde{\delta}_i &= \frac{\delta_i}{A}, \quad \xi = \frac{L_2}{L_1}, \quad \beta = \frac{EH^3 \delta_c}{12\sigma_c e L_1^4 (1-\nu^2)}, \quad \text{with } e = \exp(1). \end{aligned} \quad (5)$$

The non-dimensional form of the equilibrium equation (4) is then expressed as:

$$\beta \left[\frac{\partial^4 \tilde{w}}{\partial \tilde{x}_1^4} + \frac{2}{\xi^2} \frac{\partial^4 \tilde{w}}{\partial \tilde{x}_1^2 \partial \tilde{x}_2^2} + \frac{1}{\xi^4} \frac{\partial^4 \tilde{w}}{\partial \tilde{x}_2^4} \right] = \begin{cases} -(\tilde{\delta}_i(\tilde{x}_1, \tilde{x}_2) + \tilde{w}(\tilde{x}_1, \tilde{x}_2)) \exp[-\eta(\tilde{\delta}_i(\tilde{x}_1, \tilde{x}_2) + \tilde{w}(\tilde{x}_1, \tilde{x}_2))] & \text{if } (\tilde{\delta}_i(\tilde{x}_1, \tilde{x}_2) + \tilde{w}(\tilde{x}_1, \tilde{x}_2)) \geq 0 \\ -\frac{K_n}{e} (\tilde{\delta}_i(\tilde{x}_1, \tilde{x}_2) + \tilde{w}(\tilde{x}_1, \tilde{x}_2)) & \text{if } (\tilde{\delta}_i(\tilde{x}_1, \tilde{x}_2) + \tilde{w}(\tilde{x}_1, \tilde{x}_2)) < 0, \end{cases} \quad (6)$$

while periodic boundary conditions are applied on the edges of the film.

As apparent from (6), the solution is governed by the three non-dimensional parameters, β , η and ξ , which characterize different aspects of the film-substrate system: η accounts for the amplitude of the substrate roughness, ξ reflects the ratio of the wavelengths in the two directions and β incorporates the bending stiffness of the film. For a typical interface of transfer-printed gold film and SAM-enhanced substrate, $\beta = 5 \times 10^{-5}$, $\eta = 5 \sim 10$, and ξ depends on the choice of interface samples.

2.2. Results

As the transfer-printed film deforms under the cohesive interactions, the bending energy stored in the film increases [34]. The non-dimensional bending energy (\tilde{E}_b) can be expressed as the ratio of the energy (E_b) stored in the deformed film to the total cohesive energy (E_c) of a flat interface:

$$\tilde{E}_b = \frac{E_b}{E_c} = \frac{\beta\eta^2}{2} \int_0^1 \int_0^1 \left[\left(\frac{\partial^2 \tilde{w}}{\partial \tilde{x}_1^2} + \frac{1}{\xi^2} \frac{\partial^2 \tilde{w}}{\partial \tilde{x}_2^2} \right)^2 - \frac{(1-\nu)}{\xi^2} \left(\frac{\partial^2 \tilde{w}}{\partial \tilde{x}_1^2} \frac{\partial^2 \tilde{w}}{\partial \tilde{x}_2^2} - \left(\frac{\partial^2 \tilde{w}}{\partial \tilde{x}_1 \partial \tilde{x}_2} \right)^2 \right) \right] d\tilde{x}_1 d\tilde{x}_2, \quad (7)$$

where $E_c = e\sigma_c\delta_c L_1 L_2$ is the cohesive energy of a perfectly flat interface over an area of $L_1 \times L_2$.

Fig. 2(a) shows the variation of \tilde{E}_b with β for a fixed surface roughness $\eta = 5$ and a wavelength ratio $\xi = 1$, together with deformed profiles at four specific β values labeled A to D. The bending energy ratio curve starts at $\beta = 0$, which corresponds to a gold film with zero stiffness. At $\beta = 0$, there is no bending energy in the film and the film is perfectly attached to the substrate due to its infinite compliance. As β increases, i.e., as the film thickness increases and/or the substrate wavelength decreases, the bending energy ratio rises and reaches a maximum (in excess of 200% of the cohesive energy). Any further increase in β from B to C leads to a rapid drop in \tilde{E}_b . In this entire process, the film physically shifts from a position closely adhered to the substrate (profile B) to a quasi-unloaded configuration (profile C). Beyond this value of β at C, the bending

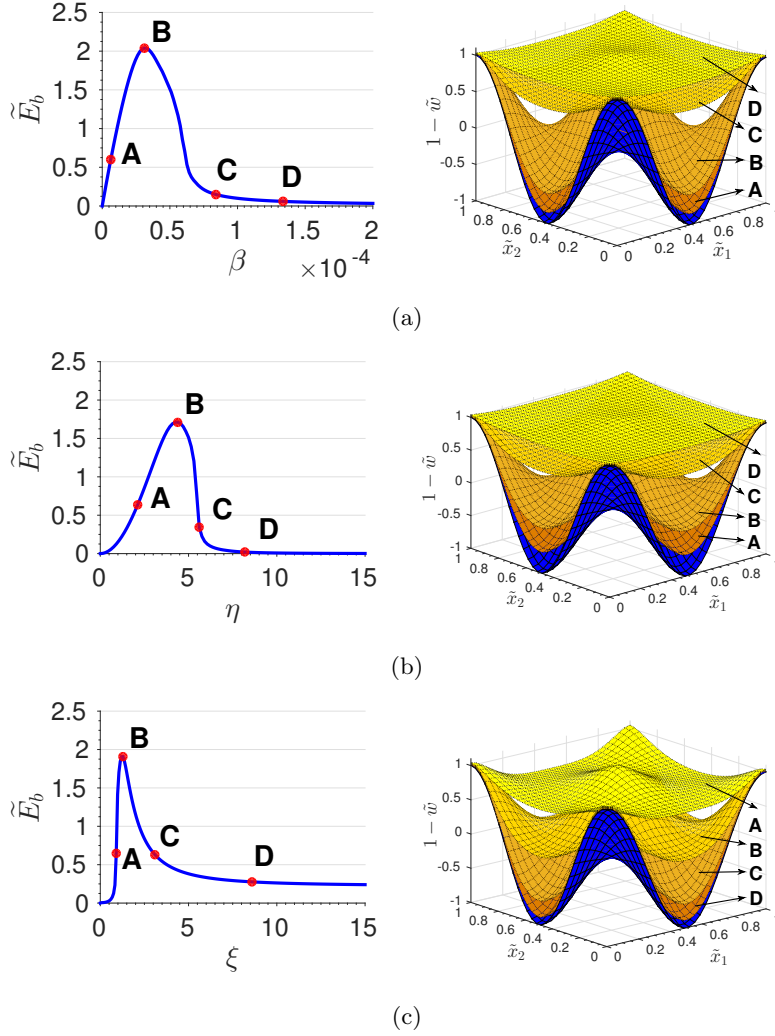
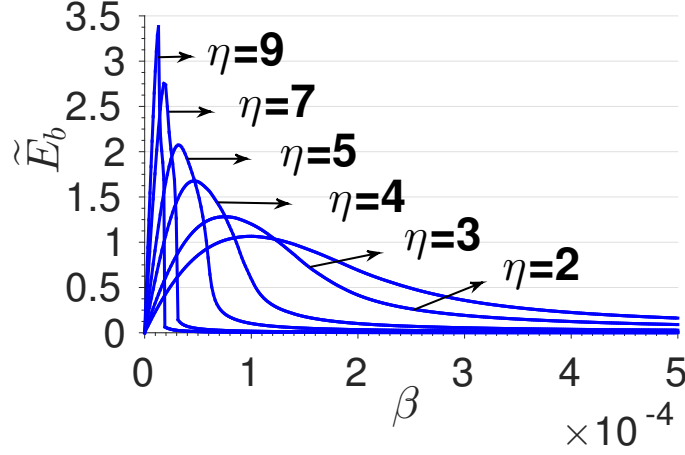


Figure 2: Effect of the non-dimensional parameters β , η , and ξ introduced in (5) on the normalized bending energy \tilde{E}_b defined in (7) for the transfer-printed film. (a) Effect of β for $\xi = 1$, $\eta = 5$; (b) Effect of η for $\beta = 5 \times 10^{-5}$ and $\xi = 1$; (c) Effect of ξ for $\beta = 5 \times 10^{-5}$ and $\eta = 5$. The right figures denote the equilibrium configurations of the film corresponding to the solutions denoted by A, B, C, and D on the left curves.

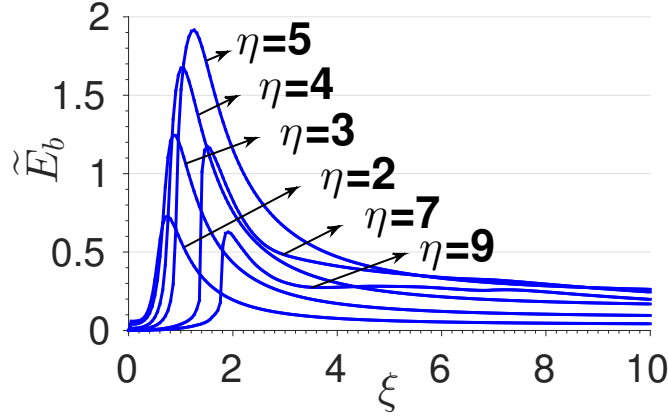
energy ratio (from point C to point D) approaches the fully unloaded profile as expected for very stiff films and/or substrates with very short wavelengths.

Figures 2(b) and 2(c) show the dependence of \tilde{E}_b with ξ and η , respectively.

Both curves exhibit similar evolution as that observed with in Fig. 2(a). It is interesting to note the behavior of \tilde{E}_b with respect to ξ in Fig. 2(c), where the film profiles change from a quasi-unloaded configuration to a position close to the substrate (A to D).



(a)



(b)

Figure 3: (a) Effect of β on bending energy ratio \tilde{E}_b for different η . The transition is abrupt for $\eta > 5$ and smooth for $\eta < 5$. (b) Effect of ξ on bending energy ratio \tilde{E}_b for different η . No abrupt changes of \tilde{E}_b occurs as ξ increases.

The dependence of \tilde{E}_b on β for different values of η with fixed $\xi = 1$ is presented in Fig. 3(a). Once again, all curves start at $\tilde{E}_b = 0$, since $\beta = 0$ corresponds to a fully compliant film, where no bending energy is stored in the film. As β increases, the bending energy increases, reaches a maximum and eventually decays to zero for high values of β , i.e., for high film stiffness or short roughness wavelength. For higher roughness ($\eta > 5$), the transition is abrupt while for smaller values of η , the β -dependence of \tilde{E}_b is smooth. A more detailed description of the dependence of the bending energy \tilde{E}_b , on the stiffness parameter β , can be found in a related work [29], which includes a discussion of the stability of the initial deformation of the transfer-printed film.

Fig. 3(b) demonstrates the evolution of \tilde{E}_b with ξ for different values of η with fixed $\beta = 5 \times 10^{-5}$. The curves start at $\tilde{E}_b = 0$, since $L_2 = 0$ when $\xi = 0$. With the increase of ξ , the bending energy increases, reaches a maximum and decays, similar to the pattern observed in Fig. 3(a). It is interesting to note that the maximum value of \tilde{E}_b does not increase monotonically with η . Rather, as the value of η increases, the maximum value of \tilde{E}_b increases and then drops with further increase in η .

3. Spallation

The initial deformed shape of the transfer-printed thin film is then used to model the spallation of the film off the SAM-enhanced substrate. The film is assumed to be rigid during spallation since the failure event happens too rapidly to cause any deformation in the film [28][35]. As the film retracts from the substrate, the cohesive interactions between the film and substrate vanish. Fig. 4(a) illustrates the spallation of a film with an initially deformed profile. In contrast, Fig. 4(b) shows the spallation of a perfectly rigid film, for which the bending stiffness is so large that there is no film deformation under cohesive tractions.

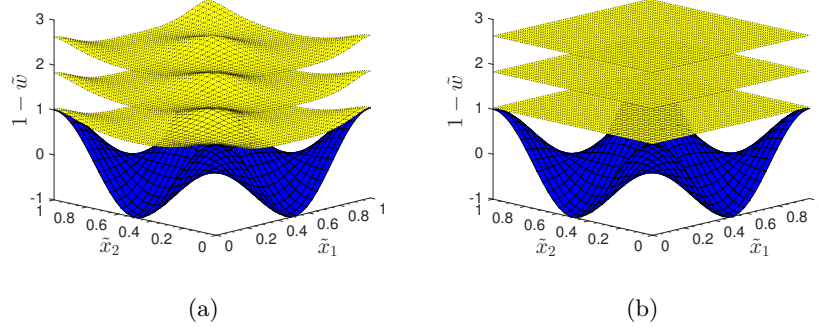


Figure 4: Schematic of two spallation models: (a) Spallation of an initially deformed film. (b) Spallation of a perfectly rigid film. In both cases, the film is assumed to be lifted rigidly from the substrate during the rapid spallation process.

3.1. Formulation

The effective cohesive traction $\bar{T}(\tilde{\delta})$ can be calculated as the average traction on the film using the non-dimensional parameters introduced in the previous section:

$$\begin{aligned}
 \bar{T}(\tilde{\delta}) &= \frac{1}{L_1 L_2} \int_0^{L_1} \int_0^{L_2} T(\tilde{\delta}, \tilde{\delta}_i(x_1, x_2)) dx_1 dx_2 \\
 &= \sigma_c \int_0^1 \int_0^1 \left\{ \tilde{\delta} + \eta[\tilde{\delta}_i(\tilde{x}_1, \tilde{x}_2) + \tilde{w}(\tilde{x}_1, \tilde{x}_2)] \right\} \exp \left\{ 1 - \tilde{\delta} - \eta[\tilde{\delta}_i(\tilde{x}_1, \tilde{x}_2) + \tilde{w}(\tilde{x}_1, \tilde{x}_2)] \right\} d\tilde{x}_1 d\tilde{x}_2
 \end{aligned} \tag{8}$$

where $\tilde{\delta} = \frac{\delta}{\delta_c}$ denotes the non-dimensional uniform displacement of the film. The effective cohesive energy, obtained by calculating the area under the effective cohesive curve, can be written as

$$\tilde{E}_c = \frac{L_1 L_2}{E_c} \int_0^\infty \bar{T}(\tilde{\delta}) d\tilde{\delta}, \tag{9}$$

where $E_c = e\sigma_c\delta_c L_1 L_2$.

3.2. Results

In addition to the effective cohesive traction of a deformable film defined by (8), the expression for the effective cohesive spallation response of a perfectly

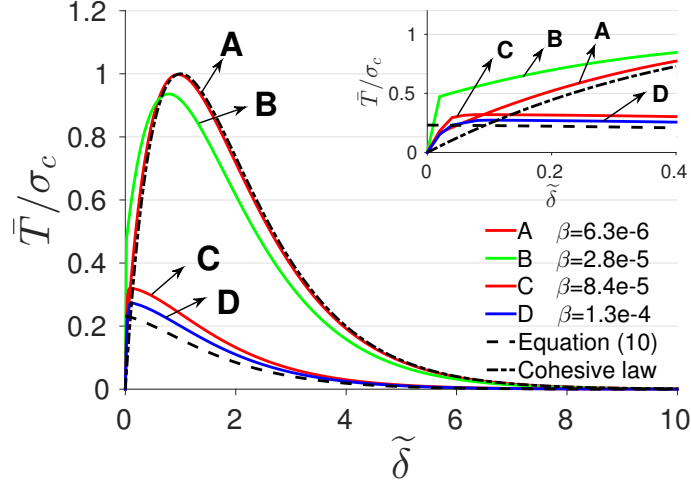
rigid film (Fig. 4(b)) can be obtained as

$$\begin{aligned}\bar{T}^R(\delta) &= \frac{1}{L_1 L_2} \int_0^{L_1} \int_0^{L_2} \frac{\sigma_c}{\delta_c} [\delta + \delta_i(x_1, x_2)] \exp \left[1 - \frac{\delta + \delta_i(x_1, x_2)}{\delta_c} \right] dx_1 dx_2 \\ &= \sigma_c \int_0^1 \int_0^1 [\tilde{\delta} + \tilde{\delta}_i(\tilde{x}_1, \tilde{x}_2)] \exp [1 - \tilde{\delta} - \tilde{\delta}_i(\tilde{x}_1, \tilde{x}_2)] d\tilde{x}_1 d\tilde{x}_2.\end{aligned}\quad (10)$$

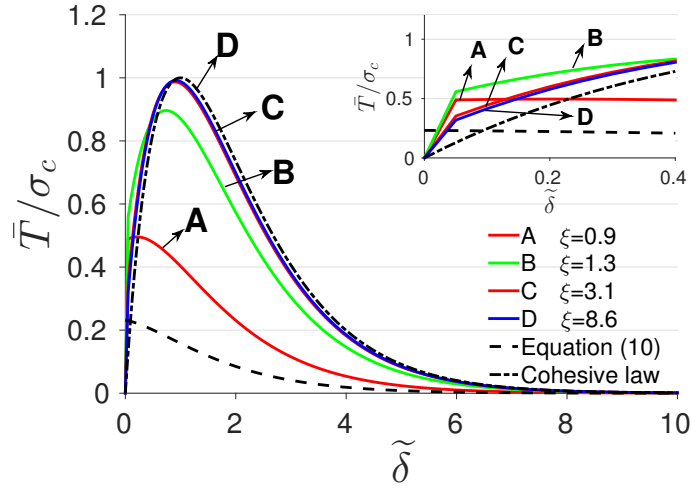
Fig. 5(a) and (b) show the effective cohesive response of the SAM-film system starting at four different initial profiles A, B, C and D, which correspond to the four points labeled in Fig. 2(a) and (c). The effective cohesive response for a perfectly rigid film and the intrinsic interfacial cohesive law are also presented for comparison. At $\tilde{\delta} = 0$, the film in the deformable case has an average traction of $\bar{T} = 0$, which corresponds to the initial equilibrium state. As $\tilde{\delta}$ increases, the film moves away from the substrate and the value of the effective cohesive traction rapidly increases before reaching the maximum. In the configuration where the film has an initial profile closely attached to the substrate, the resulting effective cohesive response (curve A in Fig. 5(a) and curve D in Fig. 5(b)) is very close to the intrinsic interface cohesive law. On the other hand, for cases where the film is initially in quasi-unloaded configurations, the effective cohesive strength is substantially smaller (by about 60%). The effective cohesive response therefore greatly depends on the initial profiles of the thin film. Note the sharp increase of the effective traction close to the region $\tilde{\delta} \rightarrow 0$ (insets of Fig. 5(a) and (b)) due to the high value of the penalty parameter K_n used to enforce contact (Eqn 3).

Fig. 6(a) and (b) respectively depict the dependence of the effective cohesive strength and cohesive energy of the film on β . The two figures have similar a pattern. The curves start at $\bar{T}_{max}/\sigma_c = 1$ and $\tilde{E}_c = 1$, where the effective interfacial cohesive response is the same as the exponential cohesive model (see Fig. 5). The cohesive strength \bar{T}_{max} and effective cohesive energy \tilde{E}_c then decrease as β increases. As the value of η increases, the decay in \bar{T}_{max} and \tilde{E}_c becomes more pronounced. As $\beta \rightarrow \infty$, the results converge to these of the perfectly rigid case.

In Fig. 7(a) and (b), the evolution of \bar{T}_{max}/σ_c and \tilde{E}_c with ξ is presented

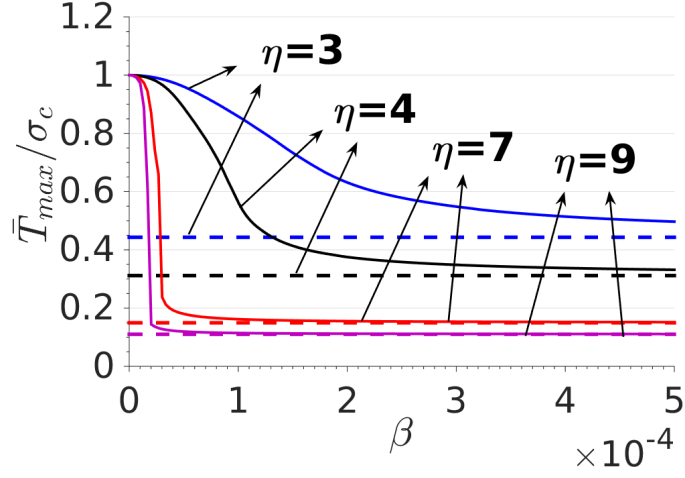


(a)

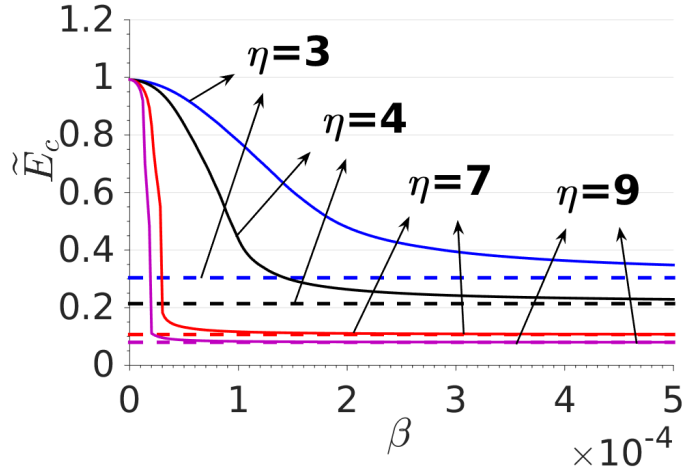


(b)

Figure 5: (a) Effective traction-separation relation for $\eta = 5$ and $\xi = 1$ with four values of β denoted by A, B, C and D (See Fig. 2(a)). (b) Effective traction-separation relation for $\eta = 5$ $\beta = 5 \times 10^{-5}$ with four values of ξ denoted by A, B, C and D (See Fig. 2(c)). The intrinsic interfacial cohesive law and the rigid film approximation are also shown for comparison. The insets show corresponding trends for small values of $\tilde{\delta}$.



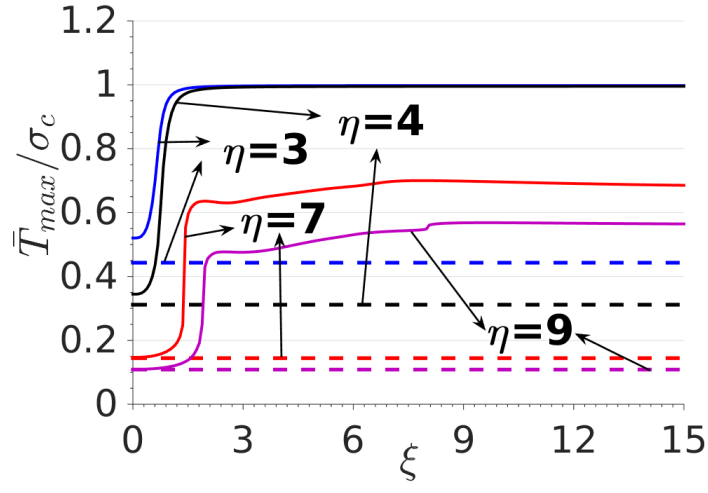
(a)



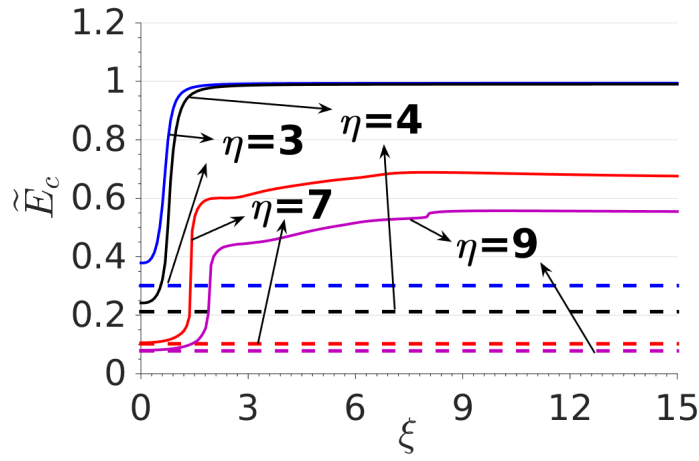
(b)

Figure 6: β -dependence of the maximum effective cohesive properties, i.e., of the cohesive strength (a) and effective cohesive energy (b) of the film, for different values of η . The result for the perfectly rigid case (Eqn (10)) is denoted by dashed horizontal lines and is the limit of the deformable case as $\beta \rightarrow \infty$.

for a fixed value of $\beta = 5 \times 10^{-5}$. Due to the compliance along L_1 direction, the curves do not start at the same value as that of a perfectly rigid case (dotted lines) at $\xi = 0$. The values of \bar{T}_{max} and \tilde{E}_c rise rather abruptly as ξ increases.



(a)



(b)

Figure 7: ξ -dependence of the effective cohesive strength (a) and cohesive energy (b) of the film for different values of η . The results for the perfectly rigid case are presented with dashed lines.

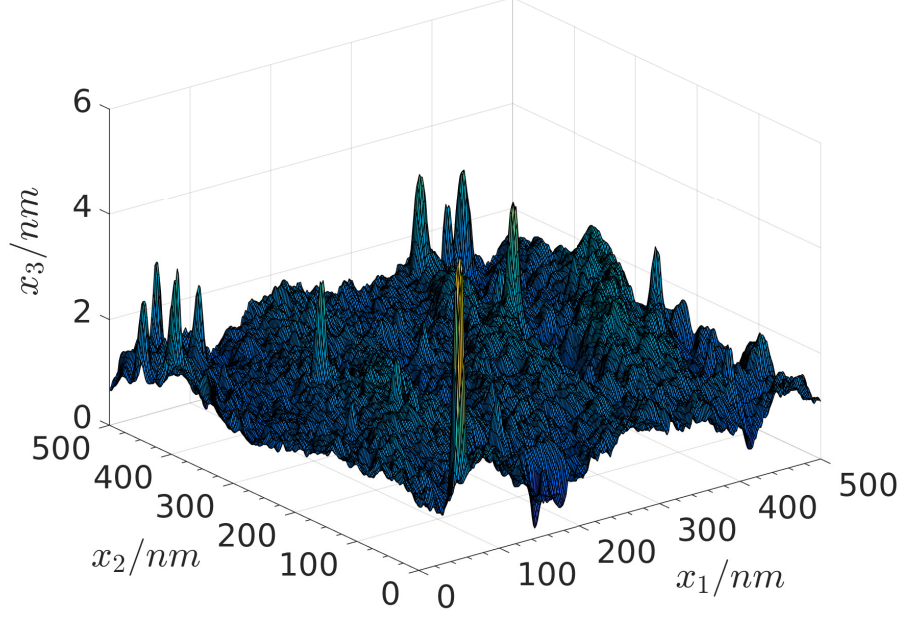


Figure 8: AFM surface profile obtained of a fused silica substrate with a dodecyltriethoxysilane (DTES) SAM layer.

4. Real Surface

As illustrated in Fig. 8, the surface profile of actual SAM-enhanced fused silica substrates is substantially more complex than the idealized harmonic roughness profile used in the previous sections. In this section, we apply the two-step approach described earlier to extract the spallation strength of actual DTES-enhanced gold/fused silica interface. For details on the preparation of the fused silica/DTES/gold system, please refer to [28].

Fig. 9(a) and (b) respectively show the profile of one $100nm \times 100nm$ sample of DTES-enhanced substrate and the deformed initial profile of the transfer-printed gold film using the combined plate/cohesive model described earlier. The roughness profile can be characterized by a wide range of surface parameters. The non-dimensional parameters η introduced earlier can be defined

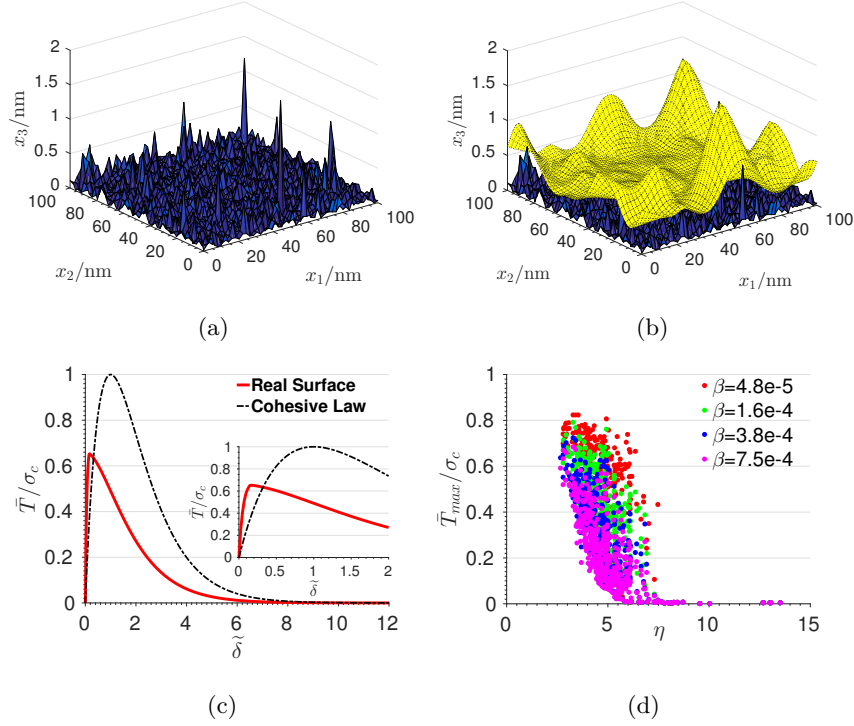


Figure 9: (a) $100\text{nm} \times 100\text{nm}$ DTES sample from the surface shown in Fig. 8. (b) Initial deformed profile of transfer-printed gold film on the DTES-enhanced substrate shown in (a). This gold film/substrate interface has $\eta = 3.5$, $\beta = 3 \times 10^{-4}$ and $\xi = 1$. (c) Effective traction-separation response for the gold film/substrate interface by applying rigid spallation to the deformed film. The intrinsic interfacial cohesive law is also presented for comparison. (d) Maximum effective cohesive traction for gold film/substrate interface of 400 randomly selected $100\text{nm} \times 100\text{nm}$ DTES-enhanced samples.

by $\eta = \frac{\max(h) - \min(h)}{2\delta_c}$, where h denotes the height of a point measured on the surface. Based on dimensional parameters $L_1 = L_2 = 100\text{nm}$ and $h_{max} - h_{min} = 1.4\text{nm}$ extracted from the surface profile in Fig. 9(a), on a film thickness $H = 45\text{nm}$, and on the cohesive parameters obtained from molecular dynamics simulations for the DTES/gold interface, $\sigma_c = 7.5 \times 10^{-10} \text{N/nm}^2$, $\delta_c = 0.2\text{nm}$, typical values of the three non-dimensional parameters introduced earlier are $\eta = 3.5$, $\beta = 4 \times 10^{-4}$ and $\xi = 1$. As shown in Fig. 9(b), the transfer-printed

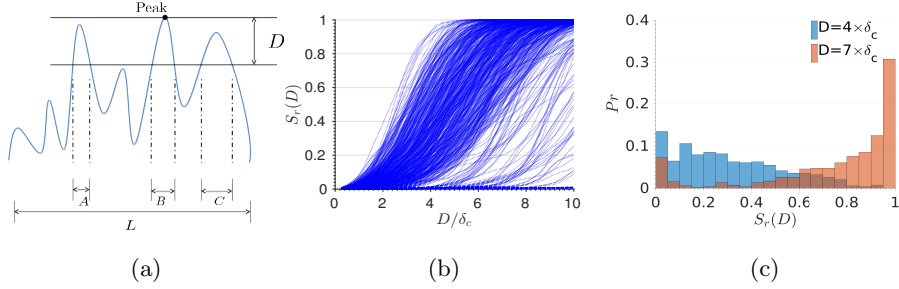


Figure 10: (a) Schematic of $S_r(D)$ for a surface profile: $S_r(D) = (A + B + C)/L$. (b) Evolution of $S_r(D)$ on D/δ_c . Each dotted line represents one surface. (c) Distribution of $S_r(D)$ for $D = 4\delta_c$ and $D = 7\delta_c$. P_r represents the ratio of number of surfaces having a particular value of $S_r(D)$ to number of surfaces in the entire sample surface collection.

film sits higher up over the peaks and deforms to adhere to the substrate in smoother areas due to the cohesive forces. Based on the initial profile of the transfer-printed film, the second step of the interface failure model, referred to previously as the rigid spallation step, is performed to obtain the effective cohesive properties of the interface. Fig. 9(c) presents the effective traction-separation response, with the exponential cohesive model for a perfectly flat interface also plotted for comparison. The effective cohesive strength \bar{T}_{max}/σ_c for this particular case is 0.68.

To assess the range of effective cohesive strength for the surface profile shown in Fig. 8, we randomly selected 400 samples of size $100nm \times 100nm$ and calculated for each profile η -dependence of the interfacial cohesive strength \bar{T}_{max} for a range of β values, i.e, for a range of film compliance values. The results are presented in Fig. 9(d). While these results clearly show a decreasing trend of \bar{T}_{max} on β and η , Fig. 9(d) clearly indicates that these two non-dimensional parameters are not sufficient to determine the effective cohesive response of the transfer-printed thin film on real surfaces.

To address this shortcoming, and in an effort to extract a surface parameter that correlates better with the effective cohesive strength, we introduce another

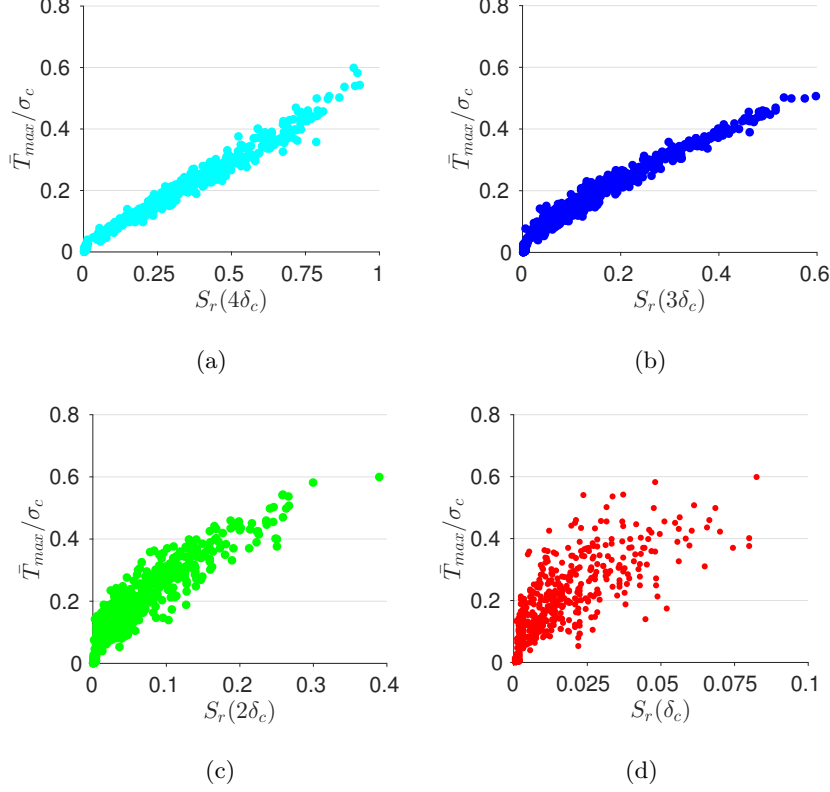


Figure 11: Evolution of \bar{T}_{max}/σ_c associated with (a) $S_r(4\delta_c)$, (b) $S_r(3\delta_c)$, (c) $S_r(2\delta_c)$ and (d) $S_r(\delta_c)$ for rigid films ($\beta \rightarrow \infty$).

parameter $S_r(D)$:

$$S_r(D) = \int_{\max(h)-D}^{+\infty} f(z)dz, \quad (11)$$

where $\max(h)$, D and $f(z)$ respectively denote the height of the surface peak, the distance from a point on the surface to the surface peak, and the surface height distribution. $S_r(D)$ is similar to the concept of bearing ratio t_p used in [36] and is schematically shown in Fig. 10(a), with $S_r(D) = \frac{A+B+C}{L}$.

Fig. 10(b) shows $S_r(D)$ for the aforementioned 400 sample surfaces. As apparent there, most surface profiles reach $S_r(D) \sim 1$ at $D = 10\delta_c$. However, for some surface with high peaks, $S_r(10\delta_c) < 1$. Fig. 10(c) presents the distribution of surface profiles with $S_r(4\delta_c)$ and $S_r(7\delta_c)$, showing that most surfaces have

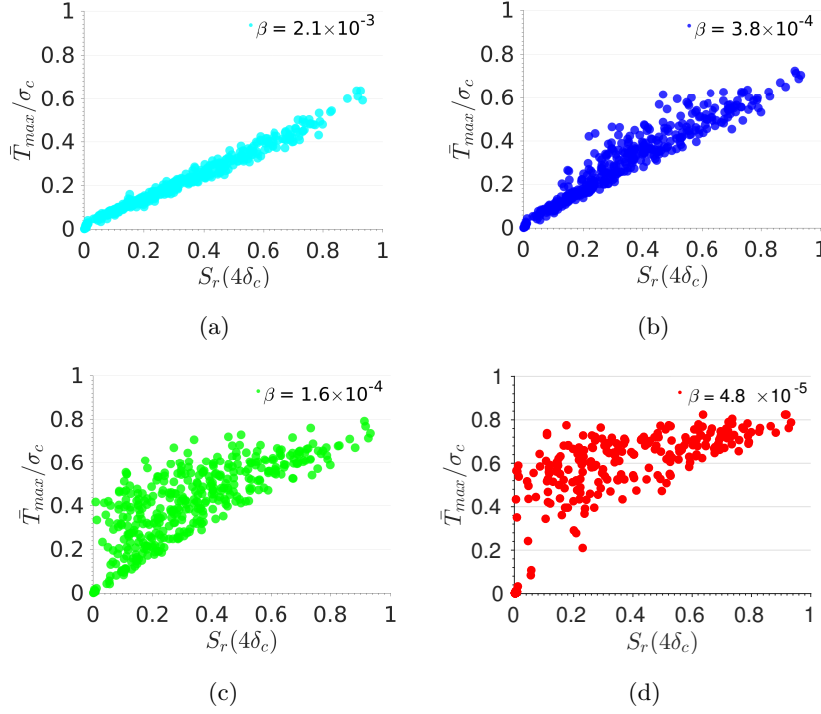


Figure 12: Evolution of \bar{T}_{max}/σ_c with $S_r(4\delta_c)$ associated with (a) $\beta = 2.1 \times 10^{-3}$, (b) $\beta = 3.8 \times 10^{-4}$, (c) $\beta = 1.6 \times 10^{-4}$ and (d) $\beta = 4.8 \times 10^{-5}$. For $\beta = 2.1 \times 10^{-3}$, the result is identical to the rigid film assumption Fig. 11(a).

$$S_r(4\delta_c) \leq 0.6 \text{ and } S_r(7\delta_c) \geq 0.6.$$

Fig. 11(a-d) presents the correlation between the effective cohesive strength \bar{T}_{max} and for values of $S_r(D)$: $S_r(4\delta_c)$, $S_r(3\delta_c)$, $S_r(2\delta_c)$ and $S_r(\delta_c)$ for a large value of β , i.e., for a high film stiffness. As shown in Fig. 11(a), \bar{T}_{max} correlates linearly with $S_r(D = 4\delta_c)$. This results is in line with the observation that the intrinsic interfacial cohesive law that underlies this study almost vanishes for a displacement jump equal and greater to $4\delta_c$ (Fig. 5). It is therefore expected that the fraction of a surface that lies within $4\delta_c$ of its peak determines the cohesive strength for a transfer-printed film with high stiffness.

As the film compliance increases, i.e., as β decreases, the linear correlation between $S_r(4\delta_c)$ and the effective cohesive strength \bar{T}_{max} decreases, as illus-

trated in Fig. 12(a-d). In other words, the compliance of the film during the transfer printing process raises the effective strength of the SAM-enhanced interface. While the surface parameter $S_r(4\delta_c)$ provides a more accurate correlation between the surface roughness and the effective cohesive strength of the SAM-enhanced interface than the η parameter used earlier in this manuscript, it is not sufficient to fully characterize the failure properties, especially for highly compliant films.

5. Conclusion

This manuscript has focused on evaluating the influence of surface roughness on effective cohesive strength of the interface between a SAM-enhanced substrate and a transfer-printed film of gold. We have employed a two-step continuum approach to link cohesive failure properties extracted from molecular dynamics for a perfectly flat interface to the effective cohesive strength of rough interfaces. The first step consisted in computing the initial profile of a deformable gold film transfer-printed on a rough SAM-enhanced substrate, with the attractive cohesive forces based on the MD model. This first step was shown to be fully described by three non-dimensional parameters. In the second step, a rigid spallation model of the film was adopted to simulate the rapid separation of the film from the substrate, thereby allowing for the computation of the effective cohesive failure relation. The two-step approach was first applied to a simplified harmonic model of the interface, then to an actual surface profile obtained with an AFM. The analysis performed on the real surface has demonstrated that surface roughness effects can reduce substantially (by sometimes more than 90%) the cohesive strength of the interface.

Acknowledgement

The financial support of the National Science Foundation (Award number 1161517) is gratefully acknowledged.

6. References

- [1] A George, D H A Blank, and J E Elshof. Nanopatterning from the gas phase: High resolution soft lithographic patterning of organosilane thin films. *Langmuir*, 25(23):13298–13301, 2009.
- [2] W Azzam, A Bashir, A Terfort, T Strunskus, and C Wöll. Combined STM and FTIR characterization of terphenylalkanethiol monolayers on Au (111): Effect of alkyl chain length and deposition temperature. *Langmuir*, 22(8):3647–3655, 2006.
- [3] J Noh, H S Kato, M Kawai, and M Hara. Surface structure and interface dynamics of alkanethiol self-assembled monolayers on Au (111). *The Journal of Physical Chemistry B*, 110(6):2793–2797, 2006.
- [4] A Ulman. Formation and structure of self-assembled monolayers. *Chemical Reviews*, 96(4):1533–1554, 1996.
- [5] M Schaeferling, S Schiller, H Paul, M Kruschina, P Pavlickova, M Meerkamp, C Giammasi, and D Kambhampati. Application of self-assembly techniques in the design of biocompatible protein microarray surfaces. *Electrophoresis*, 23(18):3097–3105, 2002.
- [6] M Mrksich, C S Chen, Y Xia, L E Dike, D E Ingber, and G M Whitesides. Controlling cell attachment on contoured surfaces with self-assembled monolayers of alkanethiolates on gold. *Proceedings of the National Academy of Sciences*, 93(20):10775–10778, 1996.
- [7] M D Losego, M E Grady, N R Sottos, D G Cahill, and P V Braun. Effects of chemical bonding on heat transport across interfaces. *Nature Materials*, 11(6):502–506, 2012.
- [8] Z Tian, A Marconnet, and G Chen. Enhancing solid-liquid interface thermal transport using self-assembled monolayers. *Applied Physics Letters*, 106(21):211602, 2015.

- [9] D K Aswal, S Lenfant, D Guerin, J V Yakhmi, and D Vuillaume. Self assembled monolayers on silicon for molecular electronics. *Analytica Chimica Acta*, 568(1):84–108, 2006.
- [10] I H Campbell, J D Kress, R L Martin, D L Smith, N N Barashkov, and J P Ferraris. Controlling charge injection in organic electronic devices using self-assembled monolayers. *Applied Physics Letters*, 71(24):3528–3530, 1997.
- [11] M P Goertz and N W Moore. Mechanics of soft interfaces studied with displacement-controlled scanning force microscopy. *Prog Surf Sci*, 85(9-12):347, 2010.
- [12] B G Bush, F W Del-Rio, C Jaye, D A Fischer, and R F Cook. Interfacial mechanical properties of alkylsilane monolayers on silicon substrates. *Journal of Microelectromechanical Systems*, 22(1):34–43, 2013.
- [13] M S Kent, ED Reedy, H Yim, A Matheson, J Sorenson, J Hall, K Schubert, D Tallant, M Garcia, T Ohlhausen, et al. Using self-assembling monolayers to study crack initiation in epoxy/silicon joints. *Journal of materials research*, 19(6):1682–1695, 2004.
- [14] A V Zhuk, A G Evans, J W Hutchinson, and G M Whitesides. The adhesion energy between polymer thin films and self-assembled monolayers. *Journal of materials research*, 13(12):3555–3564, 1998.
- [15] J I Siepmann and I R McDonald. Monte carlo simulation of the mechanical relaxation of a self-assembled monolayer. *Physical review letters*, 70(4):453, 1993.
- [16] K J Tupper and D W Brenner. Compression-induced structural transition in a self-assembled monolayer. *Langmuir*, 10(7):2335–2338, 1994.
- [17] J M D Lane, M Chandross, C D Lorenz, M J Stevens, and G S Grest. Water penetration of damaged self-assembled monolayers. *Langmuir*, 24(11):5734–5739, 2008.

- [18] R Maboudian, W R Ashurst, and C Carraro. Self-assembled monolayers as anti-stiction coatings for MEMS: characteristics and recent developments. *Sensors and Actuators A: Physical*, 82(1):219–223, 2000.
- [19] C Xu, R L Jones, and J D Batteas. Dynamic variations in adhesion of self-assembled monolayers on nanoasperities probed by atomic force microscopy. *Scanning*, 30(2):106–117, 2008.
- [20] B G Bush, F W DelRio, J Opatkiewicz, R Maboudian, and C Carraro. Effect of formation temperature and roughness on surface potential of octadecyltrichlorosilane self-assembled monolayer on silicon surfaces. *The Journal of Physical Chemistry A*, 111(49):12339–12343, 2007.
- [21] E A Weiss, R C Chiechi, G K Kaufman, J K Kriebel, Z Li, M Duati, M A Rampi, and G M Whitesides. Influence of defects on the electrical characteristics of mercury-drop junctions: Self-assembled monolayers of n-alkanethiolates on rough and smooth silver. *Journal of the American Chemical Society*, 129(14):4336–4349, 2007.
- [22] E F Douglass Jr, P F Driscoll, D Liu, N A Burnham, C R Lambert, and W G McGimpsey. Effect of electrode roughness on the capacitive behavior of self-assembled monolayers. *Analytical Chemistry*, 80(20):7670–7677, 2008.
- [23] S D Moré, H Graaf, M Baune, C Wang, and T Urisu. Influence of substrate roughness on the formation of aliphatic self-assembled monolayers (SAMs) on silicon (100). *Japanese Journal of Applied Physics*, 41(6S):4390, 2002.
- [24] K J Tupper, R J Colton, and D W Brenner. Simulations of self-assembled monolayers under compression: effect of surface asperities. *Langmuir*, 10(7):2041–2043, 1994.
- [25] K J Tupper and D W Brenner. Molecular dynamics simulations of friction in self-assembled monolayers. *Thin Solid Films*, 253(1):185–189, 1994.

- [26] R A Quon, A Ulman, and T K Vanderlick. Use of the surface forces apparatus to directly measure the influence of self-assembled monolayers on the adhesion and deformation of rough solids. *Langmuir*, 16(8):3797–3802, 2000.
- [27] A P Awasthi, M E Grady, I H Kim, N R Sottos, and P H Geubelle. Nanoscale mechanical tailoring of interfaces using self-assembled monolayers. *Mechanics of Materials*, 98:71–80, 2016.
- [28] M E Grady, P H Geubelle, P V Braun, and N R Sottos. Molecular tailoring of interfacial failure. *Langmuir*, 30(37):11096–11102, 2014.
- [29] C Zhang, A P Awasthi, P H Geubelle, M E Grady, and N R Sottos. Effects of interface roughness on cohesive strength of self-assembled monolayers. *To Appear in Applied Surface Science*.
- [30] X P Xu and A Needleman. Numerical simulations of fast crack growth in brittle solids. *Journal of the Mechanics and Physics of Solids*, 42(9):1397–1434, 1994.
- [31] M P Oday, P Nath, and W A Curtin. Thin film delamination: a discrete dislocation analysis. *Journal of the Mechanics and Physics of Solids*, 54(10):2214–2234, 2006.
- [32] V Tvergaard. Cohesive zone representations of failure between elastic or rigid solids and ductile solids. *Engineering Fracture Mechanics*, 70(14):1859–1868, 2003.
- [33] R W Soutas-Little. *Elasticity*. Courier Corporation, 1999.
- [34] G Carbone and P Decuzzi. Elastic beam over an adhesive wavy foundation. *Journal of Applied Physics*, 95(8):4476–4482, 2004.
- [35] J Wang, R L Weaver, and N R Sottos. A parametric study of laser induced thin film spallation. *Experimental Mechanics*, 42(1):74–83, 2002.

- [36] E J Abbott and F A Firestone. Specifying surface quality: a method based on accurate measurement and comparison. *Journal of Mechanical Engineering*, 55:569–572, 1933.